



# Enhanced ozonation of antibiotics using magnetic $\text{Mg}(\text{OH})_2$ nanoparticles made through magnesium recovery from discarded bischofite

Jian Lu<sup>a,\*</sup>, Qi Sun<sup>a</sup>, Jun Wu<sup>b</sup>, Guangcan Zhu<sup>c</sup>

<sup>a</sup> CAS Key Laboratory of Coastal Environmental Processes and Ecological Remediation, Yantai Institute of Coastal Zone Research (YIC), Chinese Academy of Sciences (CAS); Shandong Key Laboratory of Coastal Environmental Processes, YICCAS, Yantai, Shandong, 264003, People's Republic of China

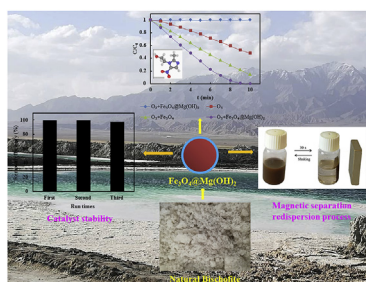
<sup>b</sup> School of Resources and Environmental Engineering, Ludong University, Yantai, Shandong, 264025, People's Republic of China

<sup>c</sup> School of Energy and Environment, Southeast University, Nanjing, Jiangsu, 210096, People's Republic of China

## HIGHLIGHTS

- $\text{Fe}_3\text{O}_4@\text{Mg}(\text{OH})_2$  magnetic nanoparticles were firstly prepared from discarded bischofite.
- Removal rate constant of MNZ increased by 7 times using  $\text{Fe}_3\text{O}_4@\text{Mg}(\text{OH})_2$  as catalyst.
- Removal rate constant only decreased by 13.2% in the third reuse run.
- Antibacterial activity of MNZ was eliminated after the catalytic ozonation.
- Mineralization efficiency of MNZ was doubled in the presence of  $\text{Fe}_3\text{O}_4@\text{Mg}(\text{OH})_2$ .

## GRAPHICAL ABSTRACT



## ARTICLE INFO

### Article history:

Received 11 July 2019

Received in revised form

23 August 2019

Accepted 26 August 2019

Available online 28 August 2019

Handling Editor: Peizhe Sun

### Keywords:

$\text{Fe}_3\text{O}_4@\text{Mg}(\text{OH})_2$  magnetic nanoparticles

Water treatment

Antibiotics

Catalytic ozonation

Core-shell structure

Antibacterial activity

## ABSTRACT

Techniques for reutilization of the discarded bischofite are limited while efficient recovery of the  $\text{Mg}(\text{OH})_2$  nanoparticles from water during the synthesis and reuse processes is a challenge. In this study, the  $\text{Fe}_3\text{O}_4@\text{Mg}(\text{OH})_2$  core-shell magnetic nanoparticles were firstly prepared from discarded bischofite and used as catalyst for improving the ozonation of metronidazole (MNZ). The removal rate constant of MNZ increased by 694.7% using  $\text{Fe}_3\text{O}_4@\text{Mg}(\text{OH})_2$ . Compared with the  $\text{Mg}(\text{OH})_2$  control, the MNZ removal rate constant of  $\text{Fe}_3\text{O}_4@\text{Mg}(\text{OH})_2$  treatment was almost tripled. The persistent high catalytic activity of the  $\text{Fe}_3\text{O}_4@\text{Mg}(\text{OH})_2$  catalyst was observed since the MNZ removal rate constant decreased by just 13.2% in the third reuse run. The  $\text{Fe}_3\text{O}_4@\text{Mg}(\text{OH})_2$  primarily enhanced ozone decomposition through producing hydroxyl radicals. The MNZ removal rate constant increased from  $0.075 \text{ min}^{-1}$  to  $0.643 \text{ min}^{-1}$  as catalyst dose increased from 0 to  $0.6 \text{ g L}^{-1}$  while it decreased by 96.0% when its initial concentration increased from 10 to  $200 \text{ mg L}^{-1}$ . The maximum removal rate constant was observed at  $25^\circ\text{C}$  when temperature increased from  $15^\circ\text{C}$  to  $35^\circ\text{C}$ . The  $\text{Cl}^-$ ,  $\text{HCO}_3^-$ ,  $\text{SO}_4^{2-}$ ,  $\text{Ca}^{2+}$ ,  $\text{Mg}^{2+}$  ions could jeopardize MNZ degradation. The antibacterial activity of MNZ was eliminated after catalytic ozonation while the mineralization efficiency was almost doubled. The nitro group reduction and the cleavage of hydroxyethyl bond were two main transformation pathways of MNZ. These findings suggest that  $\text{Fe}_3\text{O}_4@\text{Mg}(\text{OH})_2$  nanoparticle made

\* Corresponding author.

E-mail address: [jlu@yic.ac.cn](mailto:jlu@yic.ac.cn) (J. Lu).

from discarded bischofite is the promising catalyst for the ozonation of antibiotics in the terms of water purification practice and reutilization of the bischofite.

© 2019 Elsevier Ltd. All rights reserved.

## 1. Introduction

Metronidazole (MNZ) is one of nitroimidazole antibiotics which are largely consumed to treat bacterial infections for both humans and animals (Cheng et al., 2013; Fang et al., 2011; Lu et al., 2018) so that they are frequently detected from  $\text{ng L}^{-1}$  in the municipal sewage and surface water to  $\mu\text{g L}^{-1}$  in the hospital wastewater (Cheng et al., 2013). This antibiotic existing in water even at very low levels can cause significant increase in the bacterial resistance against these compounds and pose the potential hazards to human health (Khataee et al., 2017). Therefore, it is important to remove these antibiotics from the water.

It is difficult to remove MNZ using traditional methods because of its high solubility and refractory features (Cheng et al., 2013). Many techniques such as photodegradation (Dantas et al., 2010), adsorption (Rivera-Utrilla et al., 2009), and Fenton process (Cheng et al., 2013) have been used to remove MNZ from aquatic environments. Adsorption does not achieve the true degradation of MNZ (Rivera-Utrilla et al., 2009) while Fenton oxidation needs an acidic environment and photodegradation is limited by light (Cai et al., 2019; Cheng et al., 2013; Cui et al., 2016; Wang and Xu, 2012). Ozonation technology has higher oxidation efficiency but with low solubility and utilization rate of ozone (Shokri, 2015). The catalytic ozonation process utilizes catalysts to improve the ozone decomposition, enhance the generation of hydroxyl radicals, and has high oxidation efficiency and simple operation to overcome some disadvantages of ozonation (Bai et al., 2016; Huang et al., 2012; Mashayekh-Salehi et al., 2017; Shokri et al., 2016; Sun et al., 2018, 2019). Various catalysts including carbon-based nanomaterials (Bai et al., 2016; Yuan et al., 2018), porous materials (Huang et al., 2012; Ikhlaq et al., 2014), metal oxides (Khataee et al., 2017; Li et al., 2015; Mashayekh-Salehi et al., 2017; Yuan et al., 2013), hydroxides (Sun et al., 2019), and some emerging materials such as covalent organic framework (COF) (Wang et al., 2019a), bismuth oxyhalide (BIOX) (Wang et al., 2019b) and biomimetic material (Yi et al., 2019) have been used for the catalytic ozonation process. Among these materials, the magnesium hydroxide ( $\text{Mg}(\text{OH})_2$ ) is considered to be a promising ozonation catalyst because of its highly efficient activity, heavy-metals free, environmental friendliness, and low toxicity (Sun et al., 2019). However, effective separation of nano- $\text{Mg}(\text{OH})_2$  from water during the production process or recovery for reuse is still a challenge.

Magnetic separation can be used to simplify the production and recovery during the treatment process. A magnetically separable composite catalyst includes  $\text{Mg}(\text{OH})_2$  shell and a magnetic core, which can be recovered due to their magnetic properties.  $\text{Fe}_3\text{O}_4$  has been used as magnetic material in water treatment due to its easy separation from aqueous solution (Hou et al., 2013). Moreover, some wastes are used as raw materials to reduce the cost of catalyst preparation. Large quantities of natural bischofite from the salt industry are often discarded due to limited reutilizing techniques, leading to the waste of valuable magnesium resources (Sun et al., 2019), which might provide raw materials for the synthesis of  $\text{Mg}(\text{OH})_2$  materials. Few studies on the synthesis and using this kind of core-shell  $\text{Fe}_3\text{O}_4@\text{Mg}(\text{OH})_2$  composite as ozonation catalyst are reported.

This study firstly prepared the  $\text{Fe}_3\text{O}_4@\text{Mg}(\text{OH})_2$  core-shell

nanoparticles using discarded bischofite for the catalytic ozonation of antibiotics. Several key parameters including catalyst dosage, reaction temperature, inorganic ions, and initial concentration of MNZ were determined to evaluate their influence on the catalytic reaction. The stability and reusability of the catalyst, as well as the mineralization and antibacterial activity of MNZ after the catalytic ozonation were evaluated. The potential degradation pathways were also proposed. The final goal of the study was to obtain initial information on the catalytic ozonation of MNZ using  $\text{Fe}_3\text{O}_4@\text{Mg}(\text{OH})_2$  core-shell magnetic nanoparticles as promising heavy-metals-free catalyst.

## 2. Materials and methods

### 2.1. Materials and reagents

Metronidazole (MNZ) was purchased from Shanghai Macklin Biochemical Co., Ltd with purity >99%. Natural bischofite ( $\text{MgCl}_2 \cdot 6\text{H}_2\text{O}$ , magnesium chloride hexahydrate) was collected from Qarhan Salt Lake, China. Reagents (analytical grade) for catalyst synthesis including ferric chloride hexahydrate ( $\text{FeCl}_3 \cdot 6\text{H}_2\text{O}$ ), ethylene glycol, sodium acetate, ammonium hydroxide, polyethylene glycol (10000), and hexadecyltrimethylammonium bromide (CTAB) were obtained from a reagent company (Sinopharm Chemical Reagent, Shanghai, China). Acetonitrile used for high performance liquid chromatography was HPLC grade (Mreda, USA) and sodium thiosulfate used as quenching agent was analytical-purity grade. Tert-butanol (TBA) and phosphate ( $\text{PO}_4^{3-}$ ) used as hydroxyl radical scavenger were also analytical-purity grade. Superoxide dismutase (SOD) and catalase (CAT) used as  $\text{O}_2^{\cdot -}$  and  $\text{H}_2\text{O}_2$  scavenger were obtained from Beijing BioDee Biotechnology Co. Ltd and Shanghai Yuanye Biotechnology Co. Ltd, respectively. Sodium chloride, sodium bicarbonate, anhydrous sodium sulfate, and calcium chloride were analytical purity reagents and used without further purification. *Escherichia coli* (*E. coli*) was obtained from Sangon Biotech (Shanghai, China). Benzoic acid and *p*-hydroxybenzoic acid were purchased from Aladdin Bio-Chem Technology Co., Ltd (Shanghai, China). Hydrochloric acid and sodium hydroxide with analytical purity grade were used for pH adjustment.

### 2.2. Preparation of $\text{Fe}_3\text{O}_4@\text{Mg}(\text{OH})_2$ catalyst

To prepare the  $\text{Fe}_3\text{O}_4@\text{Mg}(\text{OH})_2$  magnetic nanoparticles,  $\text{Mg}(\text{OH})_2$  made from natural bischofite was layered on the magnetic particles  $\text{Fe}_3\text{O}_4$  using a direct precipitation method. The  $\text{Fe}_3\text{O}_4$  particles used as magnetic core were prepared by solvothermal reaction (Shao et al., 2012). Briefly,  $\text{FeCl}_3 \cdot 6\text{H}_2\text{O}$  (1.35 g) was dissolved in ethylene glycol (40 mL) under magnetic stirring. Then sodium acetate (3.6 g) and 1.0 g polyethylene glycol (10000) were added into the above reaction solution under vigorous stirring and the mixture was vigorously stirred for 1 h. At the end of the reaction, the obtained uniform yellow solution was transferred to a Teflon-lined stainless-steel autoclave, sealed, and heated at  $200^\circ\text{C}$ . The reaction was performed for 10 h and then the autoclave was cooled down to room temperature. The black products were washed several times with ethanol and finally dried at  $60^\circ\text{C}$  for

12 h. The obtained black powder was collected and used for the following catalytic ozonation reactions and further modification of the materials. To deposit  $\text{Mg}(\text{OH})_2$  on the magnetic  $\text{Fe}_3\text{O}_4$  particles, prepared  $\text{Fe}_3\text{O}_4$  particles (0.1 g) were ultrasonically treated with  $0.1 \text{ mol L}^{-1}$  HCl aqueous solution (50 mL) for 10 min. The magnetite particles were magnetically separated, washed with ultrapure water, and homogeneously dispersed in 30 mL of CTAB (0.15 g) solution. The mixture was sonicated for 30 min followed by the addition of 3.4 mL of  $0.5 \text{ mol L}^{-1}$   $\text{MgCl}_2 \cdot 6\text{H}_2\text{O}$  solution. The mixture was placed in a  $50^\circ\text{C}$  constant temperature bath after being stirred for 1 h at room temperature. The ammonium hydroxide (260  $\mu\text{L}$ ) was added to the above prepared solution drop by drop under constant magnetic stirring at  $50^\circ\text{C}$ . The mixture was stirred vigorously for 4 h, and then naturally cooled to room temperature. Finally, the product was separated by a magnet, rinsed with ethanol, and dried at  $60^\circ\text{C}$  for 6 h. The resulting product was the  $\text{Fe}_3\text{O}_4@\text{Mg}(\text{OH})_2$  nanoparticle. Additionally, the  $\text{Mg}(\text{OH})_2$  without being layered on  $\text{Fe}_3\text{O}_4$  was prepared for control experiment.

### 2.3. Catalytic ozonation experiments

Batch experiments were conducted in bench-scale reactors. Ozone was generated in clean oxygen by an ozonizer (Wohuan Co., Ltd). Ozone gas flow rate was regulated by a gas flowmeter and kept at  $0.1 \text{ L min}^{-1}$ . The ozone concentration was controlled by the current knob on the ozonizer. In each experiment, 100 mL of MNZ solution ( $50 \text{ mg L}^{-1}$ ) and certain amount of catalyst were added into the flask. And then ozone was continuously pumped into the solution through a glass diffuser. The samples were collected at every certain time interval, and quenched quickly by adding  $0.025 \text{ mol L}^{-1}$  sodium thiosulfate solution to remove any residual ozone. Finally, each sample was filtered through a  $0.22 \mu\text{m}$  filter for further analysis. Each test was performed in triplicate and the mean value was presented.

The catalytic potential of the synthesized  $\text{Fe}_3\text{O}_4@\text{Mg}(\text{OH})_2$  nanoparticles was assessed by degradation of MNZ in aqueous solution using catalytic ozonation process, single ozonation, and catalytic ozonation with  $\text{Mg}(\text{OH})_2$  particles and magnetic particles  $\text{Fe}_3\text{O}_4$ . Additionally, adsorption control experiments were conducted in the same flask with oxygen instead of ozone bubbling into the flask in order to discard the effect of adsorption of  $\text{Fe}_3\text{O}_4@\text{Mg}(\text{OH})_2$  nanoparticles during the experiments. The catalyst dosage was set as 0, 0.15, 0.3, 0.6, and  $1.0 \text{ g L}^{-1}$ . The temperature was adjusted by constant temperature bath to 15, 25, and  $35^\circ\text{C}$  to determine the influence of temperature on MNZ degradation. The initial concentration of MNZ was set at 10, 30, 50, 100 and  $200 \text{ mg L}^{-1}$  to explore the effect of initial concentration on MNZ removal efficiency. For discussing the effect of inorganic anions ( $\text{Cl}^-$ ,  $\text{HCO}_3^-$  and  $\text{SO}_4^{2-}$ ) on MNZ removal efficiency, a certain concentration of sodium salt (0, 0.005, 0.05, 0.2, and  $0.5 \text{ mol L}^{-1}$ ) was added into the reaction system. Similarly, a certain concentration of chloride (0, 0.005, 0.05, 0.2, and  $0.5 \text{ mol L}^{-1}$ ) was added to the reaction system when studying the effect of cations ( $\text{Ca}^{2+}$  and  $\text{Mg}^{2+}$ ) on the MNZ removal efficiency. In order to study whether the reactive oxygen species were involved in catalytic reaction, tert-butanol (TBA) ( $0.1 \text{ mol L}^{-1}$ ) and phosphate ( $\text{PO}_4^{3-}$ ) ( $0.3 \text{ mmol/L}$ ) as hydroxyl radical scavenger, superoxide dismutase (SOD) ( $>5000 \text{ u/L}$ ) and catalase (CAT) ( $>3000 \text{ u/L}$ ) used as  $\text{O}_2^{\cdot-}$  and  $\text{H}_2\text{O}_2$  scavenger, respectively, were added into catalytic ozonation system when needed (Hou et al., 2013; Zhu et al., 2017). The pH was adjusted to 3.0, 5.0, 7.0, 9.0, and 11.0 to better know the effect of pH on removal efficiency. The pH of the water samples was not adjusted except for the experiment focusing on effect of pH on MNZ removal.

In order to investigate the stability and reusability of  $\text{Fe}_3\text{O}_4@\text{Mg}(\text{OH})_2$  catalyst, the reuse experiments were also

performed. In the reuse tests, the experimental conditions were consistent with the above experiments except that the reaction was ceased after 10 min and the catalyst was collected at that time by a magnet. Considering their actual application possibility, the catalyst was directly reused for the further reaction without washing.

### 2.4. Analytical methods

The morphology of the samples was analyzed with Hitachi S-4800 field emission scanning electron microscopy (SEM, Hitachi, Japan) coupled with energy-dispersive X-ray spectroscopy (EDS). The transmission electron microscope (TEM) was recorded using JEM-1200EX (120 KV). X-ray diffraction patterns of the samples were collected on a Bruker D8 diffractometer using a  $\text{Co K}\alpha$  source, with a scan step of  $0.02^\circ$  and a scan range between  $5^\circ$  and  $90^\circ$ . Fourier transform infrared (FTIR) spectra were obtained using a FTIR spectrometer (Nicolet IS10, American). The magnetic properties of the samples were measured on a Versalab magnetometer at room temperature. X-ray photoelectron spectra (XPS) were recorded on a Thermo Scientific Escalab 250Xi X-ray photoelectron spectrometer at a pressure of about  $2 \times 10^{-9} \text{ Pa}$  with  $\text{Al K}\alpha$  X-rays as the excitation source. High-angle annular dark-field scanning transmission electron microscopy (HAADF-STEM) images, EDS line scans, and elemental mappings of the core-shell nanoparticle were obtained using a Tecnai G2 F20 S-TWIN (200 KV) HAADF-STEM microscopy. The electron paramagnetic resonance (EPR) testing of samples was performed by a Bruker-A300-10/12 electron paramagnetic resonance spectrometer. The zeta potential and size distribution of the samples were determined by Zetasizer Nano S (Malvern Instruments, Malvern, UK). Thermogravimetric analysis of the samples was obtained using a thermogravimetric analyzer under nitrogen at a heating rate of  $10^\circ\text{C min}^{-1}$ . The pH at the point of zero charge (pH<sub>zc</sub>) of the catalyst was determined by testing the zeta potential at different pH conditions using a Zetasizer Nano S (Malvern Instruments, Malvern, UK).

The concentrations of MNZ in the samples were detected by high performance liquid chromatography (HPLC, Wufeng Co., Shanghai, China) consisting of a Waters SunFire C18 reverse-phase column ( $2.1 \times 150 \text{ mm}$ ,  $3.5 \mu\text{m}$ ) with  $\text{H}_2\text{O}/\text{acetonitrile}$  (85/15, v/v %) as the mobile phase at a flow rate of  $0.2 \text{ mL min}^{-1}$ . The injection volume was  $5 \mu\text{L}$  and UV detector wavelengths were set at 315 nm. The ozone concentration was measured by the iodometric method (Flamm, 1977). The concentration of the hydroxyl radical was measured using benzoic acid (Klein et al., 1975). The total organic carbon (TOC) was determined by TOC analyzer (TOC VCPH, Shimadzu, Japan). The OD<sub>600nm</sub> was measured by ultraviolet-visible spectrophotometer (TU1810, Beijing Purkinje General Instrument Co., LTD). The intermediates of MNZ were analyzed using LCQ Fleet Liquid Chromatography-Ion Trap Mass Spectrometer (Thermo Fisher Scientific Inc., USA) equipped with Waters SunFire C18 reverse-phase column ( $2.1 \times 150 \text{ mm}$ ,  $3.5 \mu\text{m}$ ). The mobile phase was a mixture of water (90%) and acetonitrile (10%). The flow rate was  $0.1 \text{ L min}^{-1}$  and the injection volume was  $100 \mu\text{L}$ . Analyses were carried out in Electron Spray Ionization (ESI) positive ion mode with spray voltage of 5 kV, capillary temperature of  $300^\circ\text{C}$ , and the collision energy of 35 eV.

Removal data of MNZ in the presence of  $\text{Fe}_3\text{O}_4@\text{Mg}(\text{OH})_2$  were fitted by pseudo-first-order kinetic model (Eq. (1)) as the following:

$$\ln C_t = \ln C_0 - kt \quad (1)$$

where  $C_t$  is the concentration of MNZ at  $t$  min and  $C_0$  is the concentration of MNZ at the beginning;  $k$  is the rate constant of pseudo-first-order model.

The antibacterial activity of MNZ before and after the catalytic



ozonation treatment was evaluated based on its toxicity to *E. coli*. Three-fold-diluted Luria-Bertani (LB) medium was sterilized at 121 °C for 30 min and used for cultivating *E. coli*. The MNZ solution before the catalytic ozonation was added to the medium containing *E. coli* to achieve a final concentration of 50 mg L<sup>-1</sup>. The amount of the MNZ solution after the catalytic ozonation added to the medium was the same as that before catalytic ozonation. The same medium without the catalytic ozonation reaction solution was used as a control. Samples were collected at regular intervals within 24 h to measure OD600nm.

### 3. Results and discussion

#### 3.1. Characterization of synthesized Fe<sub>3</sub>O<sub>4</sub>@Mg(OH)<sub>2</sub> catalyst

After being coated with Mg(OH)<sub>2</sub> layer, small Mg(OH)<sub>2</sub> nanoplates were adhered to the surface of the Fe<sub>3</sub>O<sub>4</sub>@SiO<sub>2</sub>@Mg(OH)<sub>2</sub> composite microspheres (Fig. 1A–B). The Fe<sub>3</sub>O<sub>4</sub>@Mg(OH)<sub>2</sub> nanoparticles still maintained their spherical morphology without observed agglomeration. The Fe<sub>3</sub>O<sub>4</sub>@Mg(OH)<sub>2</sub> nanoparticles with a rough surface consisted of well-dispersed sphere with diameters ranging from 100 to 300 nm according to the SEM image. Mg and O existed on the surface of the Fe<sub>3</sub>O<sub>4</sub>@Mg(OH)<sub>2</sub> nanoparticles based on the EDS spectra (Fig. 1C–D), indicating that Mg(OH)<sub>2</sub> was successfully coated on the Fe<sub>3</sub>O<sub>4</sub> nanoparticle. Additionally, the bright outer region of the Fe<sub>3</sub>O<sub>4</sub>@Mg(OH)<sub>2</sub> nanoparticles became wider than that of the Fe<sub>3</sub>O<sub>4</sub> particles according to the TEM images (Fig. 1E and F), demonstrating the core-shell structure of the nanoparticles.

Fig. 1G showed the XRD patterns of Mg(OH)<sub>2</sub>, Fe<sub>3</sub>O<sub>4</sub> and Fe<sub>3</sub>O<sub>4</sub>@Mg(OH)<sub>2</sub>. The diffraction peaks of the synthesized Fe<sub>3</sub>O<sub>4</sub> could be identified as a cubic spinel structure (JCPDS NO. 19-0629) assigned to the (111), (220), (311), (400), (422), (551), and (440) planes. After coating with Mg(OH)<sub>2</sub>, the diffraction pattern of the resulting composite showed the characteristic diffraction of the hexagonal crystal structure of magnesium hydroxide (JCPDS NO. 7-239) assigned to the (001), (101), (102), (110), and (103) planes in addition to the Fe<sub>3</sub>O<sub>4</sub> reflections, suggesting that the Fe<sub>3</sub>O<sub>4</sub>@Mg(OH)<sub>2</sub> composites were formed. The Mg(OH)<sub>2</sub>, Fe<sub>3</sub>O<sub>4</sub>, Fe<sub>3</sub>O<sub>4</sub>@Mg(OH)<sub>2</sub> particles were also analyzed by FTIR spectroscopy throughout the range of 400–4000 cm<sup>-1</sup> (Fig. 1H). The FTIR spectrum of Mg(OH)<sub>2</sub> indicated that the sharp and intense peak at 3699 cm<sup>-1</sup> was attributed to the O–H stretching vibration in the crystal structure while the peak at 3429 cm<sup>-1</sup> was assigned to the stretching vibration of the –OH group from water molecules (physical adsorption molecules water) and the weak peak at about 440 cm<sup>-1</sup> was attributed to Mg–O stretching vibration in Mg(OH)<sub>2</sub> crystals. The FTIR spectra of Mg(OH)<sub>2</sub> were well consistent with those previously reported (Sun et al., 2019). The FTIR spectrum of Fe<sub>3</sub>O<sub>4</sub> indicated that the absorption peak at 3429 cm<sup>-1</sup> was assigned to stretching modes of O–H between molecules and 581 cm<sup>-1</sup> corresponding to stretching and bending modes of Fe–O–Fe in Fe<sub>3</sub>O<sub>4</sub> (Huang et al., 2017). The peaks at 3699 cm<sup>-1</sup>, 581 cm<sup>-1</sup>, and 440 cm<sup>-1</sup> were also detected in FTIR spectra of Fe<sub>3</sub>O<sub>4</sub>@Mg(OH)<sub>2</sub>, indicating the presence of Mg(OH)<sub>2</sub> and Fe<sub>3</sub>O<sub>4</sub> in Fe<sub>3</sub>O<sub>4</sub>@Mg(OH)<sub>2</sub> nanoparticles.

According to the magnetic hysteresis loops, the saturation magnetization values of Fe<sub>3</sub>O<sub>4</sub> and Fe<sub>3</sub>O<sub>4</sub>@Mg(OH)<sub>2</sub> nanoparticles were 70.53 and 68.73 emu/g, respectively (Fig. 1I). The saturation magnetization values of Fe<sub>3</sub>O<sub>4</sub>@Mg(OH)<sub>2</sub> nanoparticles were slightly lower than those of Fe<sub>3</sub>O<sub>4</sub> due to the deposition of the diamagnetic Mg(OH)<sub>2</sub> on the surface of Fe<sub>3</sub>O<sub>4</sub>. No residual magnetism was detected from the magnified hysteresis loops, which suggested its excellent magnetic response and magnetic stability. Moreover, the Fe<sub>3</sub>O<sub>4</sub>@Mg(OH)<sub>2</sub> nanoparticles could be homogeneously dispersed in an aqueous solution by violently

shaking or ultrasound, resulting in a dark brown suspension. The rapid aggregation from the homogenous dispersion solution was observed in the presence of external magnetic field while the redispersion happened quickly with a slight shaking once the external magnetic field was removed (Fig. 1J). These results showed that the Fe<sub>3</sub>O<sub>4</sub>@Mg(OH)<sub>2</sub> nanoparticles could be easily separated and recovered from solution by an external magnetic field, which was very important in water treatment practice.

The XPS analysis of the composite surface showed the presence of Mg, O and Fe elements on the surface of the Fe<sub>3</sub>O<sub>4</sub>@Mg(OH)<sub>2</sub> nanoparticles (Fig. 2a–c), confirming the successful coating of the Mg(OH)<sub>2</sub> on the Fe<sub>3</sub>O<sub>4</sub> particle surface. According to the Mg (1s) spectra, the peak corresponding to Mg(OH)<sub>2</sub> (located at 1302.7 eV) was identified. According to the O (1s) spectra, the peaks corresponding to O–Mg (located at 531.0 eV) and O–Fe (located at 530.0 eV) were identified. Peaks of Fe2p3/2 (located at 711.3 eV) and Fe2p1/2 (located at 724.8 eV) were also observed according to the Fe (2p) spectra to confirm the presence of the Fe<sub>3</sub>O<sub>4</sub>.

Both the high-resolution transmission electron microscopy (HRTEM) image and the HAADF-STEM image of the nanoparticles showed the contrast pattern in the central and the outer region, reconfirming the core-shell structure of the nanoparticles (Fig. 2d and e). The thickness of shell was just about 3–5 nm. The EDS line scans and the elemental mappings (Fig. 2e–h) revealed that the nanoparticle was composed of a core with Fe and a shell with Mg, which further confirmed the core-shell structure of the nanoparticle. The range of Mg was much larger than that of Fe according to the EDS line scans, indicating that Mg was in the outer layer while Fe was in the inner layer. In addition, the zeta potential of Mg(OH)<sub>2</sub>, Fe<sub>3</sub>O<sub>4</sub> and Fe<sub>3</sub>O<sub>4</sub>@Mg(OH)<sub>2</sub> was 3.67 mV, –17.2 mV and –16.4 mV, respectively (Fig. S1). The size of Mg(OH)<sub>2</sub>, Fe<sub>3</sub>O<sub>4</sub> and Fe<sub>3</sub>O<sub>4</sub>@Mg(OH)<sub>2</sub> was 400.8 nm, 251.7 nm and 291.3 nm (Fig. S2). The Mg(OH)<sub>2</sub>, Fe<sub>3</sub>O<sub>4</sub> and Fe<sub>3</sub>O<sub>4</sub>@Mg(OH)<sub>2</sub> retained a high thermostability before 200 °C (Fig. S3).

#### 3.2. Degradation of MNZ in the presence of Fe<sub>3</sub>O<sub>4</sub>@Mg(OH)<sub>2</sub> nanoparticles

The removal of MNZ in different processes was evaluated (Fig. 3a). The addition of Fe<sub>3</sub>O<sub>4</sub>, Mg(OH)<sub>2</sub> or Fe<sub>3</sub>O<sub>4</sub>@Mg(OH)<sub>2</sub> could increase the removal efficiency of MNZ in different degrees. The Fe<sub>3</sub>O<sub>4</sub>@Mg(OH)<sub>2</sub> exhibited the highest catalytic activity with the MNZ removal efficiency of 99.9% within 10 min. The removal efficiency of MNZ in the presence of Fe<sub>3</sub>O<sub>4</sub> and Mg(OH)<sub>2</sub> reached 85.6% and 87.8%, respectively, while the removal efficiency of MNZ was only 51.9% in the single ozonation process. Meanwhile, the results of adsorption tests indicated that MNZ adsorption onto Fe<sub>3</sub>O<sub>4</sub>@Mg(OH)<sub>2</sub> was just around 1% after 10 min, indicating that the increase of MNZ removal efficiency was mainly caused by the catalytic ozonation rather than adsorption by the catalysts. In order to better illustrate the catalytic performance of Fe<sub>3</sub>O<sub>4</sub>@Mg(OH)<sub>2</sub> nanoparticles on the ozonation process of MNZ, the kinetics of MNZ degradation were compared between the catalytic ozonation process and the single ozonation process using the pseudo-first-order reaction model. The pseudo-first-order kinetic model well fitted with the degradation experimental data ( $R^2 > 0.97$ ). The MNZ removal rate constant increased from 0.075 min<sup>-1</sup> to 0.185, 0.202, and 0.596 min<sup>-1</sup>, respectively when Fe<sub>3</sub>O<sub>4</sub>, Mg(OH)<sub>2</sub>, and Fe<sub>3</sub>O<sub>4</sub>@Mg(OH)<sub>2</sub> was added into the reaction system, respectively. The MNZ removal rate constant increased by 694.7% using Fe<sub>3</sub>O<sub>4</sub>@Mg(OH)<sub>2</sub> nanoparticle as the catalyst, demonstrating the remarkable catalytic performance of the synthesized Fe<sub>3</sub>O<sub>4</sub>@Mg(OH)<sub>2</sub> nanoparticle on the ozonation of MNZ. Compared with the Mg(OH)<sub>2</sub> control, the MNZ removal rate constant of Fe<sub>3</sub>O<sub>4</sub>@Mg(OH)<sub>2</sub> treatment was almost tripled, confirming the excellent

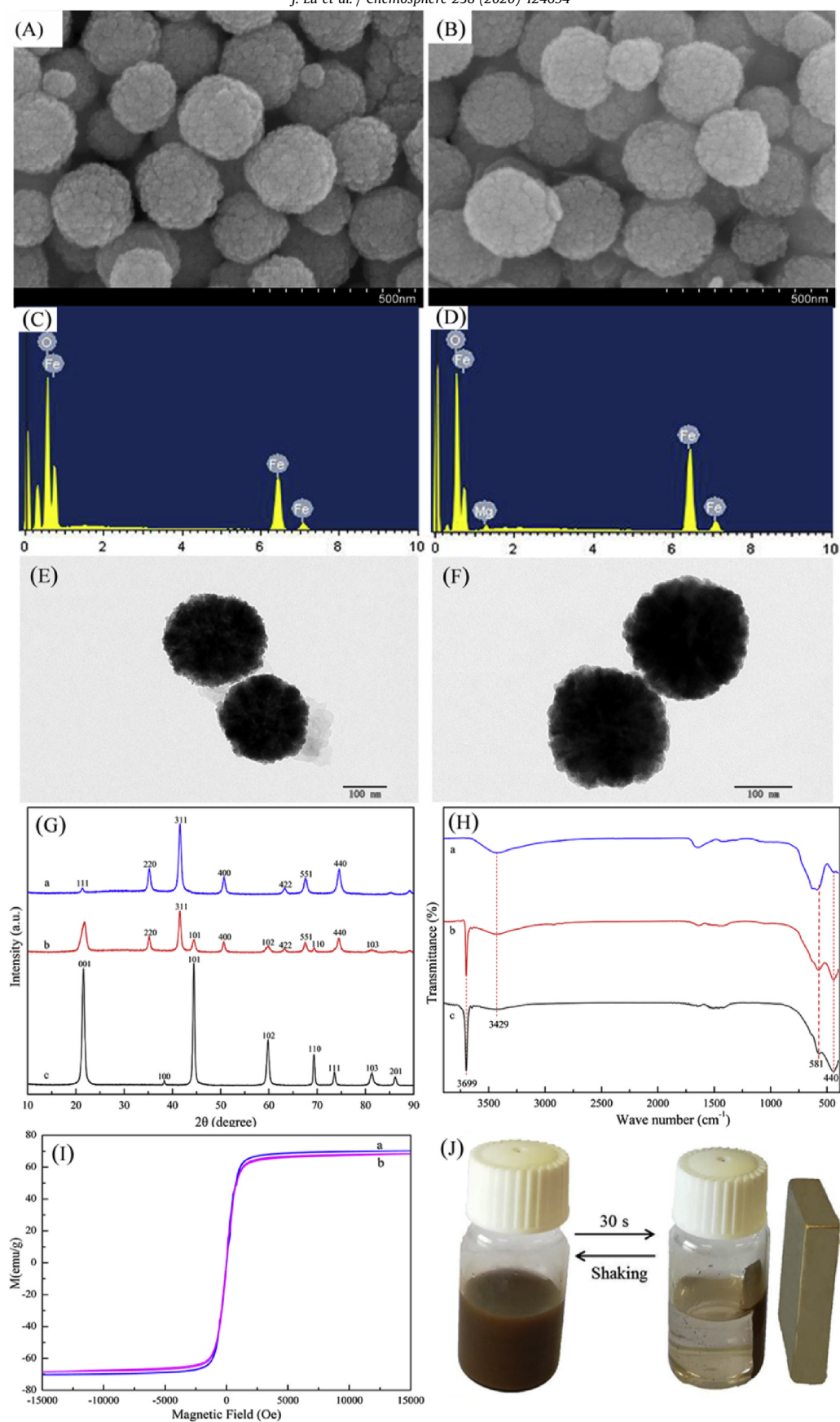


**Fig. 1.** SEM images of  $\text{Fe}_3\text{O}_4$  (A) and  $\text{Fe}_3\text{O}_4@\text{Mg}(\text{OH})_2$  (B), EDS spectra of  $\text{Fe}_3\text{O}_4$  (C) and  $\text{Fe}_3\text{O}_4@\text{Mg}(\text{OH})_2$  (D), TEM images of  $\text{Fe}_3\text{O}_4$  (E) and  $\text{Fe}_3\text{O}_4@\text{Mg}(\text{OH})_2$  (F), XRD patterns (G) of  $\text{Fe}_3\text{O}_4$  (Ga),  $\text{Fe}_3\text{O}_4@\text{Mg}(\text{OH})_2$  (Gb) and  $\text{Mg}(\text{OH})_2$  (Gc); FTIR spectra (H) of  $\text{Fe}_3\text{O}_4$  (Ha),  $\text{Fe}_3\text{O}_4@\text{Mg}(\text{OH})_2$  (Hb) and  $\text{Mg}(\text{OH})_2$  (Hc), magnetic hysteresis loops (I) of  $\text{Fe}_3\text{O}_4$  (Ia) and  $\text{Fe}_3\text{O}_4@\text{Mg}(\text{OH})_2$  (Ib), and magnetic separation-redispersion process of  $\text{Fe}_3\text{O}_4@\text{Mg}(\text{OH})_2$  (J).

catalytic performance of the  $\text{Fe}_3\text{O}_4@\text{Mg}(\text{OH})_2$  nanoparticles.  $\text{Mg}(\text{OH})_2$  combined with magnetic  $\text{Fe}_3\text{O}_4$  could not only overcome the shortcoming of single  $\text{Mg}(\text{OH})_2$  but also lead to the remarkable catalyst activity. No previous studies on the degradation of MNZ in the catalytic ozonation process with magnetic  $\text{Mg}(\text{OH})_2$  were performed to compare the results of this research work. Only the photocatalytic ozonation degradation of MNZ in water using zinc oxide nanoparticles immobilized on montmorillonite as catalyst was evaluated by Khataee et al. (2017). The results showed that MNZ was almost not degraded under UV alone while MNZ removal efficiency reached 97% under UV irradiation combined with  $\text{O}_3$  and catalyst. It is clearly observed that the prepared magnetic  $\text{Mg}(\text{OH})_2$  by this study is a very active and effective ozonation catalyst.

In order to investigate the possible reasons for the increase of MNZ removal efficiency, oxygen vacancies test were carried out for  $\text{Fe}_3\text{O}_4$ ,  $\text{Mg}(\text{OH})_2$  and  $\text{Fe}_3\text{O}_4@\text{Mg}(\text{OH})_2$  materials using EPR and the results were shown in Fig. S4. The signal of  $\text{Fe}_3\text{O}_4@\text{Mg}(\text{OH})_2$  at  $g = 2.0003$  was much stronger than that of  $\text{Fe}_3\text{O}_4$  and  $\text{Mg}(\text{OH})_2$ , which indicated that a large amount of oxygen vacancies were generated on the surface of this material. Oxygen vacancy can provide active sites for activating most of reactants and promote the decomposition of ozone, thus improving the removal efficiency of pollutants (Mathew and Juang, 2007). The BET specific surface area of  $\text{Fe}_3\text{O}_4$  was  $40.90 \text{ m}^2 \text{ g}^{-1}$  while that of the obtained material  $\text{Fe}_3\text{O}_4@\text{Mg}(\text{OH})_2$  was  $40.46 \text{ m}^2 \text{ g}^{-1}$  after loading  $\text{Mg}(\text{OH})_2$  on the surface of  $\text{Fe}_3\text{O}_4$  microspheres, indicating that the remarkable enhancement in the catalytic activity might be mainly influenced by the increase in active sites but not the high surface area of the composite material. Based on the SEM image, plenty of small  $\text{Mg}(\text{OH})_2$  nanoplates were adhered to the surface of the  $\text{Fe}_3\text{O}_4@\text{Mg}(\text{OH})_2$  composite microspheres. The loading of  $\text{Mg}(\text{OH})_2$  on the surface of  $\text{Fe}_3\text{O}_4$  led to the increase in the hydroxyl group on the surface of the  $\text{Fe}_3\text{O}_4@\text{Mg}(\text{OH})_2$  catalyst, which might subsequently enhance the catalytic ozonation of antibiotics. The hydroxyl groups on the surface of the other catalyst had been proved to be active for the hydroxyl radical production (Zhu et al., 2017).  $\text{PO}_4^{3-}$  was a hydroxyl radical scavenger that can substitute the hydroxyl radical on the catalyst surface, thus the  $\text{PO}_4^{3-}$  was selected to evaluate the role of surface hydroxyl radical. The MNZ removal rate constant decreased by half in the presence of the TBA and  $\text{PO}_4^{3-}$ , suggesting that hydroxyl radical played a critically essential role in the degradation of MNZ. Meanwhile, the concentration of the hydroxyl radical almost doubly increased from  $21.66 \mu\text{mol L}^{-1}$  to  $40.43 \mu\text{mol L}^{-1}$  with the addition of  $\text{Fe}_3\text{O}_4@\text{Mg}(\text{OH})_2$  nanoparticle (Fig. 3b), confirming the essential role of hydroxyl radical in the degradation of MNZ. In addition, the MNZ removal efficiency decreased slightly with the addition of SOD and CAT, which indicated that  $\text{O}_2^{\cdot-}$  and  $\text{H}_2\text{O}_2$  were not essential in the  $\text{Fe}_3\text{O}_4@\text{Mg}(\text{OH})_2$  catalytic ozonation process (Fig. S5). These results demonstrated the catalytic removal of MNZ in the presence of  $\text{Fe}_3\text{O}_4@\text{Mg}(\text{OH})_2$  composite was mainly due to the generation of hydroxyl radical.

Although the BET specific surface area of  $\text{Mg}(\text{OH})_2$  nanoparticles was  $35.65 \text{ m}^2 \text{ g}^{-1}$  which was much lower than that of the  $\text{Fe}_3\text{O}_4$  nanoparticles, the reaction rate constant of MNZ in the  $\text{Mg}(\text{OH})_2$  control was much higher than that of the  $\text{Fe}_3\text{O}_4$  control, confirming the relatively high catalytic activity of  $\text{Mg}(\text{OH})_2$  catalysts in comparison with  $\text{Fe}_3\text{O}_4$  and the advantage of the core-shell  $\text{Fe}_3\text{O}_4@\text{Mg}(\text{OH})_2$  magnetic composite.

The stability and reusability of the catalyst were also evaluated. The MNZ removal rate constant just decreased by 13.2% from  $0.596 \text{ min}^{-1}$  to  $0.517 \text{ min}^{-1}$  in the third run of reusing catalyst (Fig. 3c). The removal efficiency of nitroimidazole antibiotics did not sharply change after 3 runs, indicating the persistent high catalytic activity of the  $\text{Fe}_3\text{O}_4@\text{Mg}(\text{OH})_2$  nanoparticles. The relatively persistent and high catalytic activity during the reuse suggested that

$\text{Fe}_3\text{O}_4@\text{Mg}(\text{OH})_2$  nanoparticle was the promising ozonation catalyst.

### 3.3. Effect of catalyst dosage, initial MNZ concentration, initial pH, and temperature on the removal of MNZ

The influence of the dose of the prepared  $\text{Fe}_3\text{O}_4@\text{Mg}(\text{OH})_2$  nanoparticles on the removal of MNZ was investigated (Fig. 4a). The results indicated that the MNZ removal rate constant in the catalytic ozonation process increased from  $0.075 \text{ min}^{-1}$  to  $0.643 \text{ min}^{-1}$  with the increase of catalyst dose from 0 to  $0.6 \text{ g L}^{-1}$ . High dosage of catalyst can provide more active sites for oxidation reaction to subsequently cause an increased oxidation rate (Ikhlaiq et al., 2014). However, the MNZ removal rate constant had a slightly decrease after a further increase in the catalyst mass from 0.6 to  $1.0 \text{ g}$ , which might be limited by the amount of dissolved ozone (Li et al., 2015). Dosage of  $0.15 \text{ g L}^{-1}$  was chosen as the catalyst concentration in the following experiments by considering the final removal efficiency and treatment cost.

The MNZ removal under different initial concentrations varying from 10 to  $200 \text{ mg L}^{-1}$  was investigated (Fig. 4b). The removal efficiency and rate constant reduced gradually with the initial MNZ concentration increased. The degradation efficiency at initial MNZ concentration of 10, 30, 50, 100 and  $200 \text{ mg L}^{-1}$  was 98.9%, 88.0%, 64.7%, 31.4% and 18.3% after 5 min reaction, respectively. Meanwhile, the MNZ removal rate constant decreased by 96.0% from  $1.095$  to  $0.044 \text{ min}^{-1}$  when the initial concentration increased from 10 to  $200 \text{ mg L}^{-1}$ . The increase of MNZ concentration could cause the accumulation of degradation intermediates that would compete for the available oxidants against MNZ so that MNZ removal efficiency decreased (Khataee et al., 2017).

The MNZ removal rate constant increased from  $0.391 \text{ min}^{-1}$  to  $0.623 \text{ min}^{-1}$  when the pH increased from 3.0 to 7.0 (Fig. 4c). The MNZ removal rate constant decreased by 30.9% when pH further increased from 7.0 to 11.0, suggested that the MNZ removal was inhibited under alkaline conditions. The  $\text{pH}_{\text{ZC}}$  of the  $\text{Fe}_3\text{O}_4@\text{Mg}(\text{OH})_2$  catalyst was measured as 6.7 in this experiment. The hydroxyl group on the catalyst surface which is active for the hydroxyl radical production could become protonated or deprotonated when the solution pH is lower than or greater than its  $\text{pH}_{\text{ZC}}$  (Zhu et al., 2017). For this reason, the MNZ removal was inhibited under both acidic and alkaline conditions. Most of the surface hydroxyl groups existed in a neutral state when the solution pH increased from 3.0 to 7.0, which led to increase in the MNZ removal efficiency. On the other hand, the catalytic activity was inhibited by the deprotonated catalyst under alkaline conditions (at pH 9.0 or 11.0), which led to the decrease in the MNZ removal efficiency.

The MNZ removal rate constant sharply increased from  $0.367 \text{ min}^{-1}$  to  $0.596 \text{ min}^{-1}$  as the temperature rose from  $15$  to  $25^\circ\text{C}$  (Fig. 4d). However, MNZ removal efficiency was suppressed when temperature further increased up to  $35^\circ\text{C}$ . The removal rate constant decreased by 32.9% to  $0.373 \text{ min}^{-1}$  when the temperature increased from  $25^\circ\text{C}$  to  $35^\circ\text{C}$ . Generally, the MNZ removal efficiency could be directly improved because a relatively high temperature should reduce the reaction activation energy and then increase the rate of chemical reaction and mass transfer (Huang et al., 2012). Besides, the solubility of ozone decreased in aqueous solution as the temperature increased (Huang et al., 2012), which reduced the generation of hydroxyl radicals and would subsequently depress the removal of MNZ. The joint results of two opposite effects made reaction temperature of  $25^\circ\text{C}$  exert a positive effect on the MNZ decay.



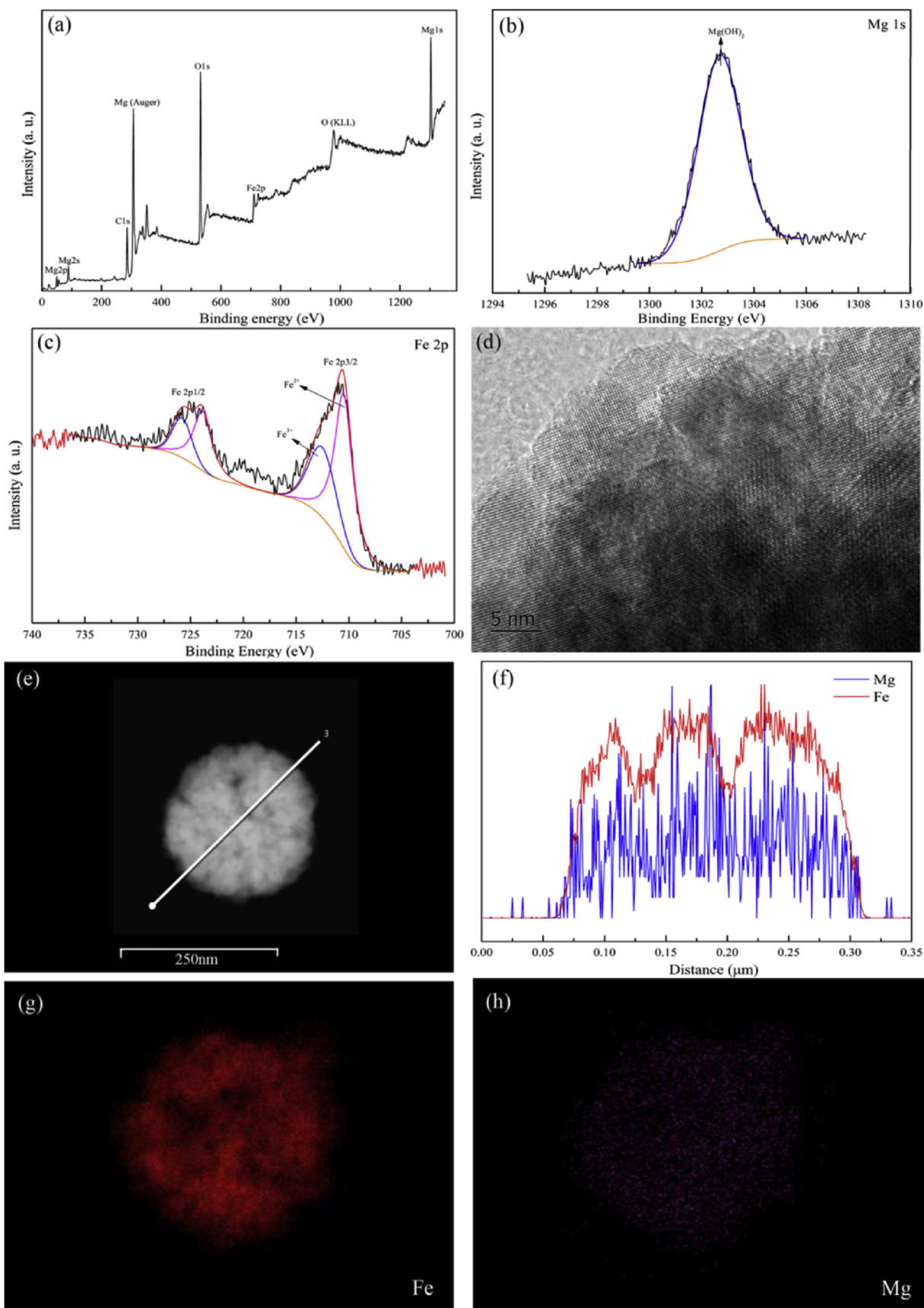


**Fig. 2.** X-ray photoelectron spectroscopy (XPS) investigations of the  $\text{Fe}_3\text{O}_4@\text{Mg}(\text{OH})_2$ , survey scan (a), Mg 1s (b), Fe 2p (c), HRTEM image (d), HAADF-STEM image (e), EDS line scans (f), and the elemental mappings of Fe (g) and Mg (h).

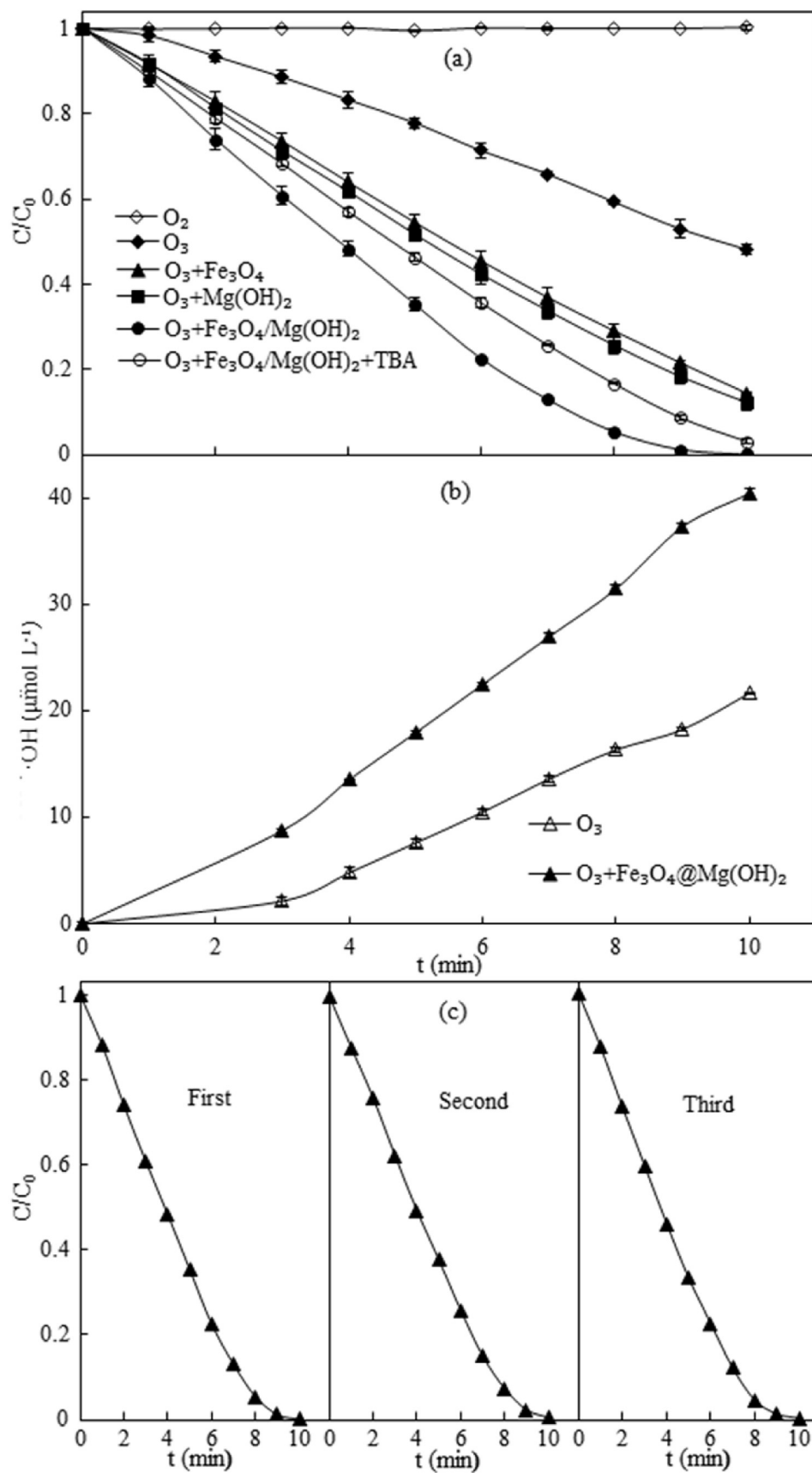


Fig. 3. Comparison of metronidazole removal in different processes (a), evolution of the hydroxyl radical in the ozonation system after the addition of benzoic acid of  $1g L^{-1}$ , and catalytic ozonation performance of the catalyst in successive runs (c).



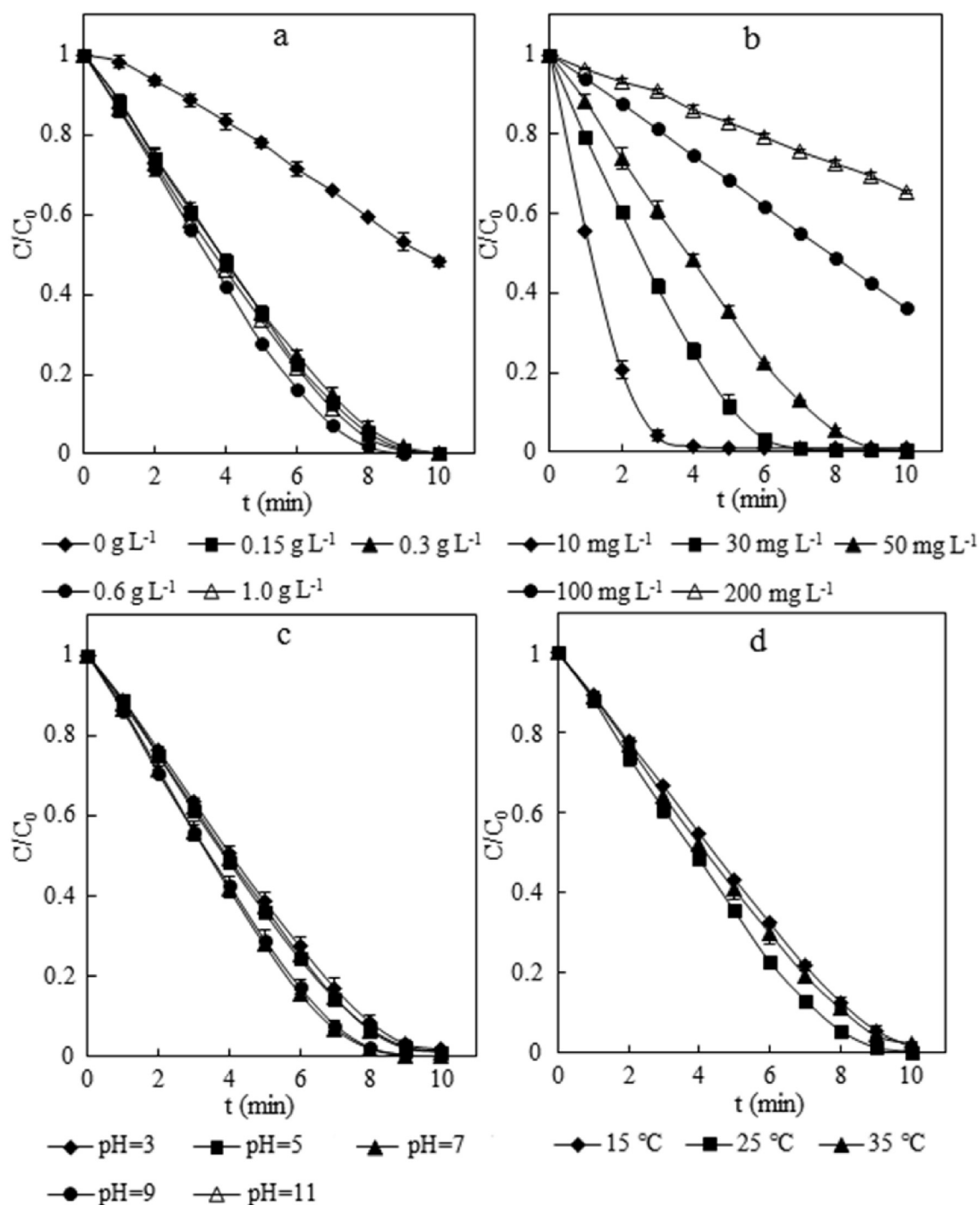


Fig. 4. Effect of catalyst dosage (a), initial concentration (b), initial pH (c), and reaction temperature (d) on the removal of metronidazole.

### 3.4. Effect of anions and cations on the removal of MNZ

The inhibitory effect on MNZ removal was observed when the anions including  $\text{Cl}^-$ ,  $\text{HCO}_3^-$ , and  $\text{SO}_4^{2-}$  were introduced into the reaction system (Fig. 5a–c). Increase of the bicarbonate resulted in the decrease of MNZ degradation efficiency. The removal rate constant of MNZ decreased by 88.7% with increased concentration of bicarbonate from 0 to 0.5 mol L<sup>-1</sup>. The removal rate constant of MNZ decreased by 58.6% and 87.0% when the initial concentration of  $\text{Cl}^-$  and  $\text{SO}_4^{2-}$  increased from 0 to 0.5 mol L<sup>-1</sup>, respectively. These anions possessing high affinity for surface active sites of catalysts

can rapidly occupy the reaction site, which subsequently reduces the ozone decomposition and catalytic efficiency of the catalyst (Yuan et al., 2013). The MNZ removal rate constant decreased by 47.1% when the initial  $\text{Ca}^{2+}$  concentration increased from 0 to 0.5 mol L<sup>-1</sup> while that decreased by 49.0% when the initial  $\text{Mg}^{2+}$  concentration increased from 0 to 0.5 mol L<sup>-1</sup> (Fig. 5d and e). The decrease in the reaction rate of MNZ might be caused by the capture of  $\cdot\text{OH}$  by the coexistent chloride ions since  $\text{Ca}^{2+}$  and  $\text{Mg}^{2+}$  belong to alkali metal with stable valences without participating the degradation reaction (Song et al., 2016).

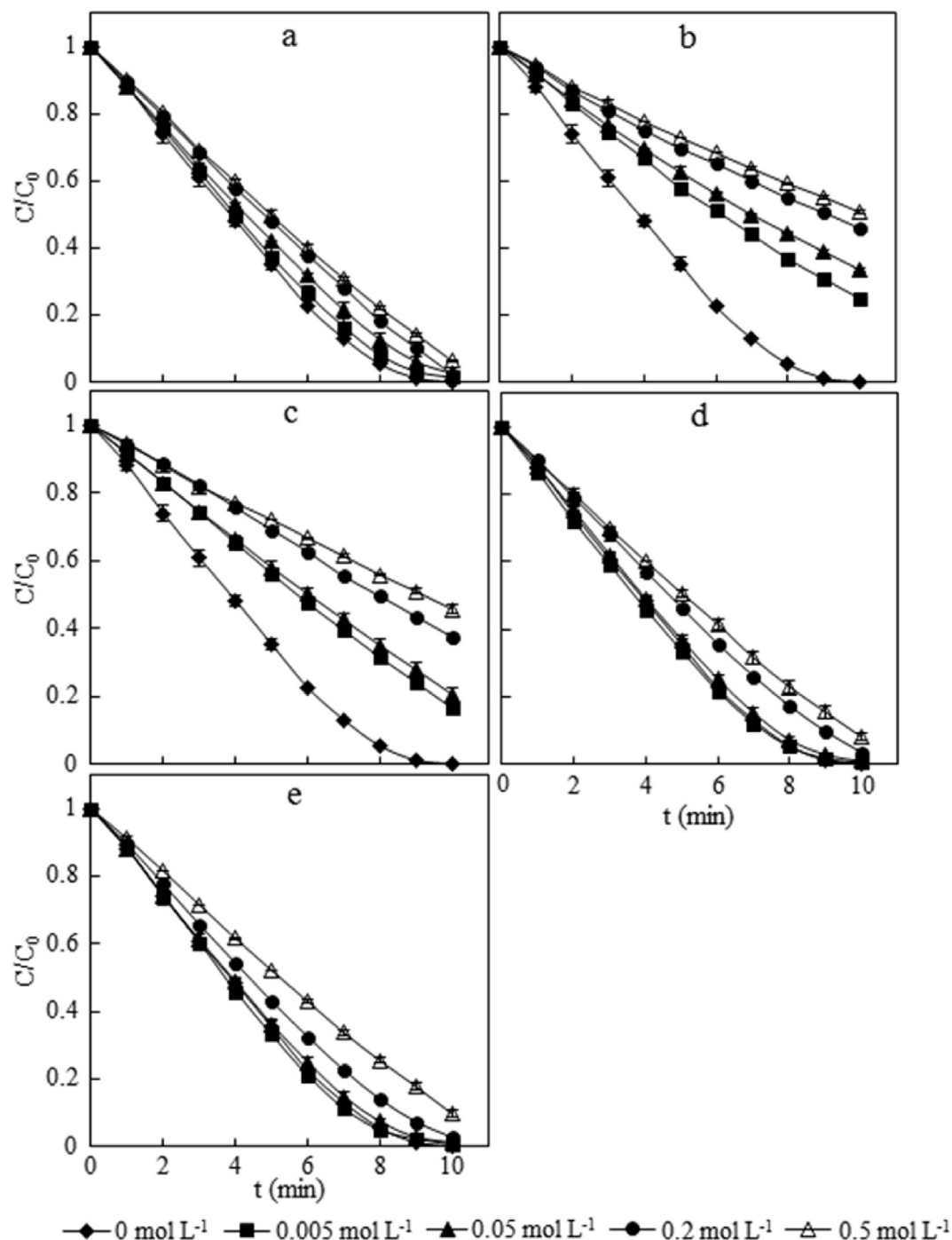
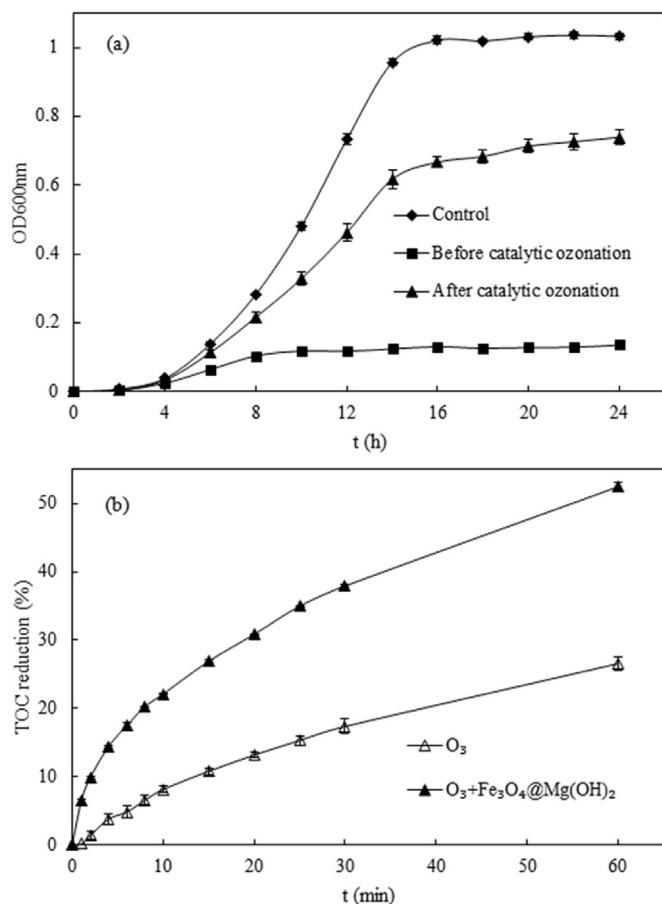


Fig. 5. Effect of inorganic anions including  $\text{Cl}^-$  (a),  $\text{HCO}_3^-$  (b), and  $\text{SO}_4^{2-}$  (c) as well as inorganic cations including  $\text{Ca}^{2+}$  (d) and  $\text{Mg}^{2+}$  (e) on the degradation of metronidazole.

### 3.5. Effect of catalytic ozonation on the antibacterial activity and mineralization of MNZ

The antibacterial activity of MNZ before and after the catalytic ozonation treatment was discussed (Fig. 6a). The growth of *E. coli* was severely inhibited in the presence of MNZ ( $50 \text{ mg L}^{-1}$ ) while that in the medium containing catalytic ozonation treatment solution or the control medium was almost comparable, suggesting that the MNZ had lost its antibacterial activity after the catalytic ozonation. Similar observation was reported during the cathode degradation of MNZ (Kong et al., 2015).

The TOC removal was also evaluated to understand the mineralization efficiency of MNZ under catalytic ozone oxidation (Fig. 6b). More than half of TOC (52.4%) was removed in the presence of  $\text{Fe}_3\text{O}_4@\text{Mg}(\text{OH})_2$  nanoparticles within 60 min while only 26.6% of TOC was removed in the single ozonation process. The mineralization efficiency was almost doubled, indicating the remarkable enhancement of MNZ mineralization in the presence of  $\text{Fe}_3\text{O}_4@\text{Mg}(\text{OH})_2$  nanoparticles. This result also indirectly illustrated that the addition of the catalyst accelerated the generation of hydroxyl radicals and accordingly the removal rate of TOC was accelerated in the catalytic ozonation degradation of MNZ in



**Fig. 6.** Effect the catalytic ozonation treatment on the antibacterial activity against *Escherichia coli* (a) and mineralization (b) of metronidazole. To evaluate antibacterial activities before and after the catalytic ozonation, water samples were collected at 0 and 10 min in the catalytic ozonation system, respectively.

aqueous solution.

### 3.6. Degradation pathways of MNZ during the catalytic ozonation

The intermediates of the catalytic ozonation of MNZ determined by high performance liquid chromatography-mass spectrometry (HPLC-MS) method were shown in Table S1. Overall, three degraded products including 2-methyl-5-nitroimidazole ( $m/z$  128), 1-(2-hydroxyethyl)-2-methyl-5-hydroxylamine imidazole ( $m/z$  158), and 1-(2-hydroxyethyl)-2-methyl-5-aminoimidazole ( $m/z$  140) were tentatively identified with molecular weights lower than MNZ ( $m/z$  172). The possible degradation pathways of MNZ during catalytic ozonation could be inferred in Fig. 7 based on the HPLC-MS analysis data and previous study on the oxidation pathway of MNZ (Kong et al., 2015; Wang et al., 2017). The main transformation mechanisms might include the nitro group reduction and the cleavage of hydroxyethyl bond.

## 4. Conclusion

The Fe<sub>3</sub>O<sub>4</sub>@Mg(OH)<sub>2</sub> core-shell magnetic nanoparticles made from natural bischofite were firstly used as a heterogeneous ozonation catalyst for degradation of MNZ. Mg(OH)<sub>2</sub> combined with magnetic Fe<sub>3</sub>O<sub>4</sub> could not only overcome the shortcoming of single Mg(OH)<sub>2</sub> but also lead to the remarkable catalyst activity. The removal rate constant of MNZ increased by almost 7 times using

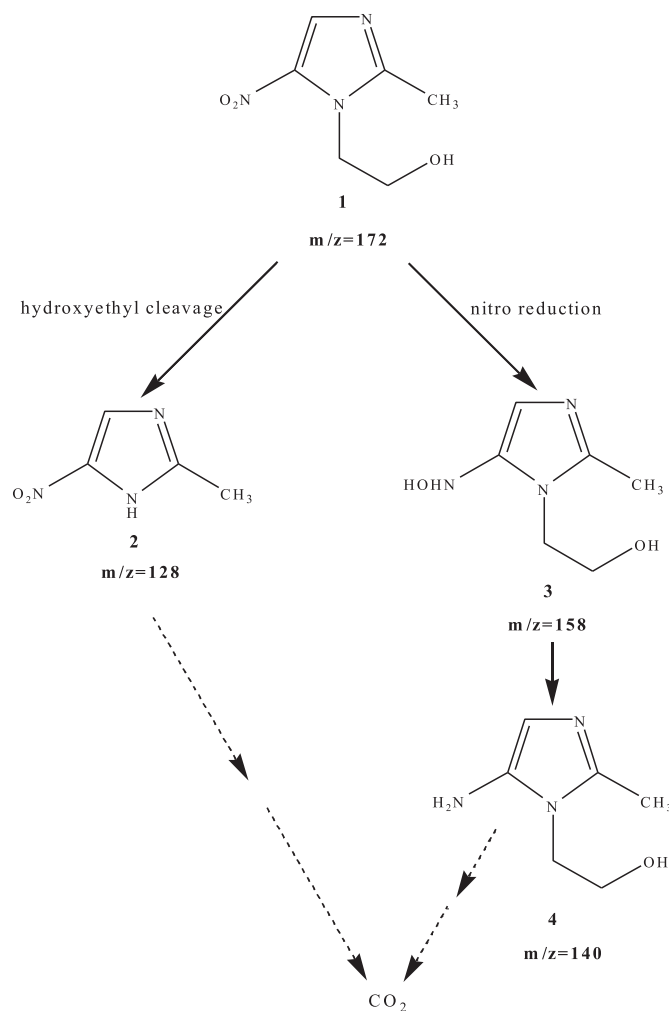


**Fig. 7.** Proposed transformation pathways of catalytic ozonation degradation of MNZ. Metronidazole (No. 1,  $m/z$  172), 2-methyl-5-nitroimidazole (No. 2,  $m/z$  128), 1-(2-hydroxyethyl)-2-methyl-5-hydroxylamine imidazole (No. 3,  $m/z$  158), 1-(2-hydroxyethyl)-2-methyl-5-aminoimidazole (No. 4,  $m/z$  140).

Fe<sub>3</sub>O<sub>4</sub>@Mg(OH)<sub>2</sub> nanoparticles as heavy metal-free catalyst. Compared with the Mg(OH)<sub>2</sub> control, the MNZ removal rate constant of Fe<sub>3</sub>O<sub>4</sub>@Mg(OH)<sub>2</sub> treatment was almost tripled. The inhibition of the hydroxyl radical scavenger on the catalytic ozonation suggested that the hydroxyl radical reaction might be the predominant removal process. The catalyst dosage, reaction temperature, initial MNZ concentration, inorganic anions (Cl<sup>-</sup>, HCO<sub>3</sub><sup>-</sup> and SO<sub>4</sub><sup>2-</sup>), inorganic cations (Ca<sup>2+</sup> and Mg<sup>2+</sup>), and initial pH had important influences on the catalytic ozonation of MNZ. The relatively persistent and high catalytic activity of the Fe<sub>3</sub>O<sub>4</sub>@Mg(OH)<sub>2</sub> nanoparticles was observed during reuse process. The catalytic ozonation led to the loss of antibacterial activity of MNZ. The mineralization efficiency was almost doubled in the presence of Fe<sub>3</sub>O<sub>4</sub>@Mg(OH)<sub>2</sub> nanoparticles. The nitro group reduction and the cleavage of hydroxyethyl bond might be the main ozonation transformation pathways of MNZ in the presence of Fe<sub>3</sub>O<sub>4</sub>@Mg(OH)<sub>2</sub> nanoparticles. These findings suggest that Fe<sub>3</sub>O<sub>4</sub>@Mg(OH)<sub>2</sub> nanoparticle made from discarded bischofite is the promising catalyst for the ozonation of antibiotics for water treatment practice and magnesium reutilization of the discarded bischofite in salt industry.

## Acknowledgements

This work was supported by National Natural Science Foundation of China (No. 41877131), Taishan Scholar Program of Shandong Province (No. tsqn201812116), One Hundred Talents Program of Chinese Academy of Sciences (Y629041021), and Two-Hundred Talents Plan of Yantai (Y739011021).

## Appendix A. Supplementary data

Supplementary data to this article can be found online at <https://doi.org/10.1016/j.chemosphere.2019.124694>.

## References

- Bai, Z.Y., Yang, Q., Wang, J.L., 2016. Fe<sub>3</sub>O<sub>4</sub>/multi-walled carbon nanotubes as an efficient catalyst for catalytic ozonation of p-hydroxybenzoic acid. *Int. J. Environ. Sci. Technol.* 13, 483–492.
- Cai, W.W., Peng, T., Zhang, J.N., Hu, L.X., Yang, B., Yang, Y.Y., Chen, J., Ying, G.G., 2019. Degradation of clindazole by UV/chlorine process: kinetics, transformation pathway and toxicity evaluation. *Chemosphere* 219, 243–249.
- Cheng, W., Yang, M., Xie, Y., Liang, B., Fang, Z., Tsang, E.P., 2013. Enhancement of mineralization of metronidazole by the electro-Fenton process with a Ce/SnO<sub>2</sub>-Sb coated titanium anode. *Chem. Eng. J.* 220 (11), 214–220.
- Cui, C., Jin, L., Jiang, L., Han, Q., Lin, K., Lu, S., Zhang, D., Cao, G., 2016. Removal of trace level amounts of twelve sulfonamides from drinking water by UV-activated peroxymonosulfate. *Sci. Total Environ.* 572, 244–251.
- Dantas, R.F., Rossiter, O., Teixeira, A.K.R., Simoes, A.S.M., da Silva, V.L., 2010. Direct UV photolysis of propranolol and metronidazole in aqueous solution. *Chem. Eng. J.* 158, 143–147.
- Fang, Z., Chen, J., Qiu, X., Qiu, X., Cheng, W., Zhu, L., 2011. Effective removal of antibiotic metronidazole from water by nanoscale zero-valent iron particles. *Desalination* 268, 60–67.
- Flamm, D.L., 1977. Analysis of ozone at low concentrations with boric acid buffered potassium iodide. *Environ. Sci. Technol.* 11, 978–983.
- Hou, L., Zhang, H., Wang, L., Chen, L., 2013. Ultrasound-enhanced magnetite catalytic ozonation of tetracycline in water. *Chem. Eng. J.* 229, 577–584.
- Huang, R., Lan, B., Chen, Z., Yan, H., Zhang, Q., Bing, J., Li, L., 2012. Catalytic ozonation of p-chlorobenzoic acid over MCM-41 and Fe loaded MCM-41. *Chem. Eng. J.* 180, 19–24.
- Huang, Y., Xu, W., Hu, L., Zeng, J., He, C., Tan, X., He, Z., Zhang, Q., Shu, D., 2017. Combined adsorption and catalytic ozonation for removal of endocrine disrupting compounds over MWCNTs/Fe<sub>3</sub>O<sub>4</sub> composites. *Catal. Today* 297, 143–150.
- Ikhlaq, A., Brown, D.R., Kasprzyk-Hordern, B., 2014. Catalytic ozonation for the removal of organic contaminants in water on ZSM-5 zeolites. *Appl. Catal. B Environ.* 154–155, 110–122.
- Khataee, A., Kiranşan, M., Karaca, S., Sheydaei, M., 2017. Photocatalytic ozonation of metronidazole by synthesized zinc oxide nanoparticles immobilized on montmorillonite. *J. Taiwan Inst. Chem. E.* 74, 196–204.
- Klein, G.W., Bhatla, K., Madhavan, V., Schuler, R.H., 1975. Reaction of OH with benzoic acid. Isomer distribution in the radical intermediates. *J. Phys. Chem.* 79, 1767–1774.
- Kong, D., Liang, B., Yun, H., Cheng, H., Ma, J., Cui, M., Wang, A., Ren, N., 2015. Cathodic degradation of antibiotics: characterization and pathway analysis. *Water Res.* 72, 281–292.
- Li, G., Lu, Y., Lu, C., Zhu, M., Zhai, C., Du, Y., Yang, P., 2015. Efficient catalytic ozonation of bisphenol-A over reduced graphene oxide modified sea urchin-like  $\alpha$ -MnO<sub>2</sub> architectures. *J. Hazard Mater.* 294, 201–208.
- Lu, J., Wu, J., Zhang, C., Zhang, Y., Lin, Y., Luo, Y., 2018. Occurrence, distribution, and ecological-health risks of selected antibiotics in coastal waters along the coastline of China. *Sci. Total Environ.* 644, 1469–1476.
- Mashayekh-Salehi, A., Moussavi, G., Yaghmaei, K., 2017. Preparation, characterization and catalytic activity of a novel mesoporous nanocrystalline MgO nanoparticle for ozonation of acetaminophen as an emerging water contaminant. *Chem. Eng. J.* 310, 157–169.
- Mathew, D.S., Juang, R.S., 2007. An overview of the structure and magnetism of spinel ferrite nanoparticles and their synthesis in microemulsions. *Chem. Eng. J.* 129, 51–65.
- Rivera-Utrilla, J., Prados-Joya, G., Sanchez-Polo, M., Ferro-Garcia, M.A., Bautista-Toledo, I., 2009. Removal of nitroimidazole antibiotics from aqueous solution by adsorption/bioadsorption on activated carbon. *J. Hazard Mater.* 170, 298–305.
- Shao, M., Ning, F., Zhao, J., Wei, M., Evans, D.G., Duan, X., 2012. Preparation of Fe<sub>3</sub>O<sub>4</sub>@SiO<sub>2</sub>@Layered double hydroxide core-shell microspheres for magnetic separation of proteins. *J. Am. Chem. Soc.* 134, 1071–1077.
- Shokri, A., 2015. Degradation of 2-nitrophenol from petrochemical wastewater by ozone. *Russ. J. Appl. Chem.* 88, 2038–2043.
- Shokri, A., Mahanpoor, K., Soodbar, D., 2016. Degradation of Ortho-Toluidine in petrochemical wastewater by ozonation, UV/O<sub>3</sub>, O<sub>3</sub>/H<sub>2</sub>O<sub>2</sub> and UV/O<sub>3</sub>/H<sub>2</sub>O<sub>2</sub> processes. *Desalin Water Treat* 57, 16473–16482.
- Song, C., Wang, L., Ren, J., Lv, B., Sun, Z., Yan, J., Li, X., Liu, J., 2016. Comparative study of diethyl phthalate degradation by UV/H<sub>2</sub>O<sub>2</sub> and UV/TiO<sub>2</sub>: kinetics, mechanism, and effects of operational parameters. *Environ. Sci. Pollut. Res.* 23, 2640–2650.
- Sun, P., Li, Y., Meng, T., Zhang, R., Song, M., Ren, J., 2018. Removal of sulfonamide antibiotics and human metabolite by biochar and biochar/H<sub>2</sub>O<sub>2</sub> in synthetic urine. *Water Res.* 147, 91–100.
- Sun, Q., Zhu, G., Wu, J., Lu, J., Zhang, Z., 2019. Catalytic ozonation of nitroimidazole antibiotics using nano-magnesium hydroxide as heavy-metals free catalyst. *Desalin Water Treat* 161, 216–227.
- Wang, J.L., Xu, L.J., 2012. Advanced oxidation processes for wastewater treatment: formation of hydroxyl radical and application. *Crit. Rev. Environ. Sci. Technol.* 42, 251–325.
- Wang, X., Liu, P., Ma, J., Liu, H., 2017. Preparation of novel composites based on hydrophilized and functionalized polyacrylonitrile membrane-immobilized NZVI for reductive transformation of metronidazole. *Appl. Surf. Sci.* 396, 841–850.
- Wang, H., Zeng, Z., Xu, P., Li, L., Zeng, G., Xiao, R., Tang, Z., Huang, D., Tang, L., Lai, C., Jiang, D., Liu, Y., Yi, H., Qin, L., Ye, S., Ren, X., Tang, W., 2019a. Recent progress in covalent organic framework thin films: fabrications, applications and perspectives. *Chem. Soc. Rev.* 48, 488–516.
- Wang, Z., Chen, M., Huang, D., Zeng, G., Xu, P., Zhou, C., Lai, C., Wang, H., Cheng, M., Wang, W., 2019b. Multiply structural optimized strategies for bismuth oxyhalide photocatalysis and their environmental application. *Chem. Eng. J.* 374, 1025–1045.
- Yi, H., Yan, M., Huang, D., Zeng, G., Lai, C., Li, M., Huo, X., Qin, L., Liu, S., Liu, X., Li, B., Wang, H., Shen, M., Fu, Y., Guo, X., 2019. Synergistic effect of artificial enzyme and 2D nano-structured Bi<sub>2</sub>WO<sub>6</sub> for eco-friendly and efficient biomimetic photocatalysis. *Appl. Catal. B Environ.* 250, 52–62.
- Yuan, R., Zhou, B., Hua, D., Shi, C., 2013. Enhanced photocatalytic degradation of humic acids using Al and Fe co-doped TiO<sub>2</sub> nanotubes under UV/ozonation for drinking water purification. *J. Hazard Mater.* 262, 527–538.
- Yuan, X., Qin, W., Lei, X., Sun, L., Li, Q., Li, D., Xu, H., Xia, D., 2018. Efficient enhancement of ozonation performance via ZVZ immobilized g-C<sub>3</sub>N<sub>4</sub> towards superior oxidation of micropollutants. *Chemosphere* 205, 369–379, 2018.
- Zhu, H., Ma, W., Han, H., Han, Y., Ma, W., 2017. Catalytic ozonation of quinoline using nano-MgO: Efficacy, pathways, mechanisms and its application to real biologically pretreated coal gasification wastewater. *Chem. Eng. J.* 327, 91–99.